

Extracting Off-Diagonal Order from Diagonal Basis Measurements

Bo Xiao,^{1,*} Javier Robledo Moreno,^{1,2,†} Matthew Fishman,¹ Dries Sels,^{1,2} Ehsan Khatami,³ and Richard Scalettar⁴

¹*Center for Computational Quantum Physics, Flatiron Institute,
162 Fifth Avenue, New York, New York 10010 USA*

²*Department of Physics, New York University, New York, New York 10003, USA*

³*Department of Physics and Astronomy, San José State University, San José, CA 95192 USA*

⁴*Department of Physics and Astronomy, University of California, Davis, CA 95616 USA*

(Dated: August 9, 2024)

Quantum gas microscopy has developed into a powerful tool to explore strongly correlated quantum systems. However, discerning phases with topological or off-diagonal long range order requires the ability to extract these correlations from site-resolved measurements. Here, we show that a multi-scale complexity measure can pinpoint the transition to and from the bond ordered wave phase of the one-dimensional extended Hubbard model with an off-diagonal order parameter, sandwiched between diagonal charge and spin density wave phases, using only diagonal descriptors. We study the model directly in the thermodynamic limit using the recently developed variational uniform matrix product states algorithm, and draw our samples from degenerate ground states related by global spin rotations, emulating the projective measurements that are accessible in experiments. Our results will have important implications for the study of exotic phases using optical lattice experiments.

Introduction.— Quantum gas microscopy for ultracold atoms in optical lattices, in which high-resolution real-space snapshots of the many-body system are accessible, is a prominent tool for studying strongly-correlated systems [1–3]. These projective measurements can be analyzed ‘by hand’ with traditional counting to compute observables, both local or extended spin and charge correlations [4–8]. The snapshots are often termed ‘diagonal’ since they comprise measurements of density observables $n_{i\sigma} = \langle c_{i\sigma}^\dagger c_{i\sigma} \rangle$, where $c_{i\sigma}^\dagger$ ($c_{i\sigma}$) is the spin- σ fermion creation (destruction) operator at site i , which have matching row and column indices of the Greens function G_{ii}^σ .

The same is true for the outcome of large-scale programmable quantum simulators based on Rydberg atoms, which allow arranging a large number of qubits in arbitrary lattice geometries and controlling the Hamiltonian evolution of the system [9–15]. A crucial open question is whether the fact that these experiments do not at present capture ‘off-diagonal’ information encoded in the full G_{ij}^σ will limit the insight they can yield.

Recent advances in machine learning methods [16–18] hold promise for answering this question. Convolutional neural networks and hybrid supervised-unsupervised approaches have been used to classify quantum gas microscopy data in emulations of the two-dimensional Fermi-Hubbard model [19], to visualize and identify multi-particle diagonal correlations [20, 21], and to detect new diagonal ordered phases in Rydberg atom quantum simulators [22]. Momentum-space images of cold atoms have also been analyzed to identify quantum phase transitions [23, 24].

Machine learning methods are able to capture order parameters or relevant thermodynamic quantities in classical as well as quantum systems, and therefore, detect symmetry-breaking phases [25–32]. In contrast, it is

much harder to identify topological phase transitions involving off-diagonal long range order. In the realm of classical statistical physics, the two-dimensional XY and q-state clock models have been investigated to identify Berezinskii-Kosterlitz-Thouless (BKT) transitions [33–35]. However, much less is known for BKT-type *quantum* phase transitions.

The simplest context in which this issue can be explored is that of quasi-one-dimensional materials, e.g. organic conductors, carbon nanotubes [37–41], for which the one-dimensional extended Hubbard model is a minimal description [42–47]:

$$H = -t \sum_{i,\sigma} \left(c_{i,\sigma}^\dagger c_{i+1,\sigma} + c_{i+1,\sigma}^\dagger c_{i,\sigma} \right) + U \sum_i n_{i,\uparrow} n_{i,\downarrow} + V \sum_{i,\sigma\sigma'} n_{i,\sigma} n_{i+1,\sigma'}, \quad (1)$$

where U and V are on-site and nearest-neighbor Coulomb interactions and $t = 1$ sets the unit of energy. An infinitesimally small U drives a transition to a regime with quasi-long range spin order [47]. We will refer to this as a ‘SDW’, but emphasize that the ground state spin correlations decay as a power law. Similarly, an infinitesimally small V induces charge density wave (CDW) order with staggered empty and doubly occupied sites [47]. However, much less obvious is the existence, between these two phases, of a narrow bond ordered wave (BOW) region with alternating large and small kinetic energy on adjacent sites, and a BKT-type transition separating it from the SDW phase [36, 45, 48–53] (see Fig. 1 (c)). Converged results on the exact location of this BKT-type transition have not been obtained [54–57]. The model thus offers a unique opportunity to test machine learning tools for examining subtle quantum phase transitions characterized by non-diagonal order.

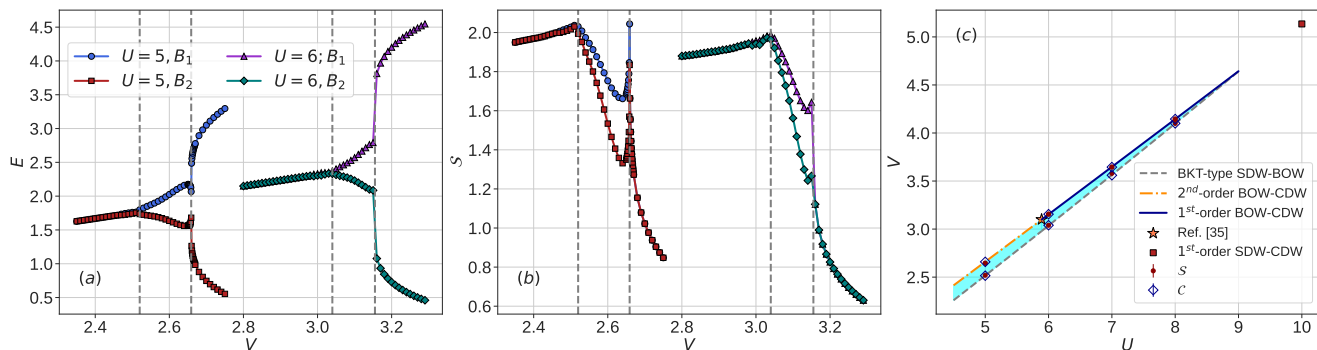


FIG. 1. (a) Energy E_i on two bonds B_i ($i = 1, 2$) associated with one two-site unit cell and (b) von Neumann entanglement entropy \mathcal{S}_i computed via partitioning along these two bonds vs. nearest-neighbor interaction V at fixed $U = 5$ and $U = 6$. (c) Phase diagram of the one-dimensional extended Hubbard model at half filling in the $U - V$ plane. Phase boundaries are determined using the structural complexity \mathcal{C} (blue diamond) and corroborated by the entanglement entropy \mathcal{S} (red circle) at select U 's. The blue shaded region denotes the BOW phase which is characterized by off-diagonal long-range order. Orange star indicates a tri-critical point where the nature of BOW-CDW transition switches from second-order to first-order, based on Ref [36]. The red square indicates a direct first-order transition from SDW to CDW at $U = 10$, determined using the structural complexity \mathcal{C} . Bond dimension $\mathcal{D} = 2000$ is employed.

In this paper, we use the state-of-the-art variational uniform matrix product states (VUMPS) algorithm [58–60] to obtain the ground state of the model at half filling, directly in the thermodynamic limit (TDL). We then emulate projective and diagonal measurements on optical lattice experiments by sampling spin-resolved occupancy snapshots from the VUMPS wavefunction. These snapshots are first analysed using principal component analysis (PCA), and then using a recently proposed *structural complexity* measure [61, 62]. We find that while PCA accurately captures the first and second order transitions between the BOW and CDW phases and the associated CDW order parameter, it fails to identify differences between the SDW and BOW samples. The structural complexity, on the other hand, starts off with a long *bitstring* consisting of concatenated samples and through a series of coarse-graining steps, is able to deduce the location of both transitions.

Variational uniform matrix product states.— Inspired by tangent space ideas [58, 63, 64], VUMPS optimizes a translational invariant matrix product state (MPS) directly in the TDL, in contrast to the more traditional infinite size density matrix renormalization group (iDMRG) [65–67] algorithm which starts from a small system and grows the state one site at a time.

Similar to DMRG, the energy minimization problem is reformulated as a series of local eigenvalue problems of effective Hamiltonians projected into the MPS basis. In practice a linear solver is used to perform the sum of the formally infinite number of Hamiltonian terms to obtain the effective Hamiltonians. By working directly with a translational invariant ansatz in VUMPS, we can remove the solitonic excitation induced by the use of open boundary conditions [55, 57]. In practice, all of our VUMPS calculations of the extended Hubbard model use a single-

site update with a two-site unit cell, and we constrain our states to conserve $U(1)$ particle number and spin projection symmetry [59, 69]. We also constrain our states to be in the $S_z = 0$ symmetry sector. Results of convergence with bond dimension are shown in the Supplemental Materials [68].

Fig. 1 (a) shows the energy E on two bonds B_i ($i = 1, 2$) that are associated with a two-site unit cell, computed using VUMPS. It shows clear signals of both phase transitions. For each fixed U , energies E_1 and E_2 inside one unit cell are exactly equal to each other in the SDW phase when V is small. As V is gradually increased, E_1 and E_2 split, which reflects the broken translational symmetry of the BOW phase. The phase boundary between SDW and BOW can be determined quantitatively by setting a small threshold, e.g., where $|E_1 - E_2| \sim 10^{-5}$. As V is further increased, the smooth or sudden changes in the energy per bond characterize the second-order ($U = 5$) or first-order ($U = 6$) phase transitions from BOW to CDW.

We can use the two bonds in a unit cell to partition the infinite system into two half-infinite subsystems and compute the von Neumann entanglement entropy \mathcal{S}_i . As shown in Fig. 1(b), in the BOW phase, \mathcal{S}_i has different values computed using different partitionings. This corresponds to the spontaneously dimerized phase of the spin chain and the \mathbb{Z}_2 degeneracy of the two types of polarization [36, 52]. In sharp contrast, the entanglement entropies computed in different ways of partitioning have exactly the same value in the SDW and CDW phases. Therefore, the point where entanglement entropies deviate from one another can be used to locate the BOW phase boundaries, which gives results consistent with those obtained from the two energies.

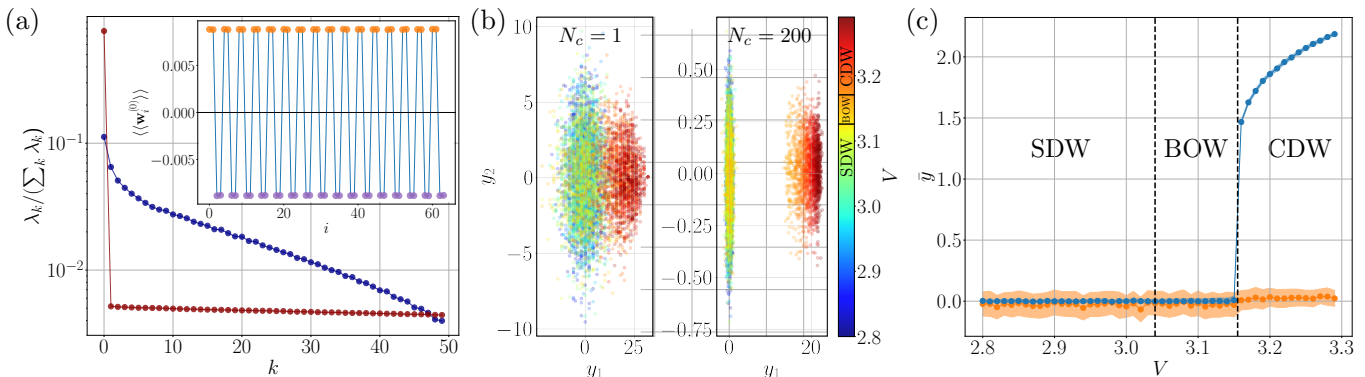


FIG. 2. Principal component analysis of the samples generated at $U = 6$ and different values of $V \in [2.8, 3.3]$ in a uniform grid with separation $\Delta V = 0.1$. (a) The relative weight of the eigenvalues of the covariance matrix for two values of concatenated samples N_c (see [68]). The inset shows the amplitude of the first principal component for $N_c = 200$, averaged over the concatenated samples. (b) Projection of the input features to the first two principal components both when $N_c = 1$ and $N_c = 200$. The color indicates the value of V to which each projected feature belongs. (c) Average projection of the input features corresponding to a fixed V to the first (blue) and second (orange) principal components for $N_c = 200$. The shaded region shows the variance of the average, measuring the spread of the projected input features at a fixed V . Vertical dashed lines indicate the phase transition points obtained from the entanglement entropy.

Sampling— We obtain our emulated experimental data by sampling finite subsystems of the translational invariant states found by VUMPS. To obtain a sample, we repeat the tensors of the unit cell, and sample the resulting subsystem as one would sample a finite MPS [70, 71]. More specifically, we start by tracing our system down to a single site and sampling from the resulting density matrix, projecting onto the local state that was found and iterating the procedure over the finite subsystem. The unit cell is repeated sixteen times, providing samples that correspond to a chain of length $L = 32$ sites. For each value of U and V , $N_s = 50000$ samples are collected. The sampled spin-resolved occupancy is stored in a feature array \mathbf{x} of length $2L$, where even and odd entries represent the spin-up and spin-down occupancy for each lattice site.

Spontaneous symmetry breaking considerations— The states found by VUMPS spontaneously break the $SU(2)$ symmetry of the model, and the spin direction of the state found by VUMPS will depend on details of the optimization, such as the initial state. Therefore, getting multiple samples from the same state obtained by VUMPS can be biased by the arbitrary spin direction of the state. To reduce this effect, we apply a random local $SU(2)$ spin rotation uniformly to each site of the state before we obtain each sample.

While the continuous $SU(2)$ symmetry is restored when producing the samples, the discrete \mathcal{Z}_2 symmetry present in BOW and CDW phases is broken in the VUMPS wave function [see Fig. 1 (a) and 1(b)]. Even if the experimental procedure does not break the \mathcal{Z}_2 symmetry in the CDW phase (the wave function is the homogeneous linear combination of both configurations), each individual sample will reflect which of the two ground states

it comes from. There, the symmetry can be explicitly broken by post processing the samples, i.e., by translating by one site those that do not share the same pattern. Furthermore, the use of an even number of lattice sites, together with open boundary conditions (as commonly done in experiments) will break the \mathcal{Z}_2 symmetry in the BOW phase. Open boundary conditions effectively provide a pinning field in the kinetic energy, forcing the strong bonds to be adjacent to the edges of the lattice [57] (see [68] for a demonstration using exact diagonalization on chains of finite length). Therefore, the conclusions obtained with our emulated projective measurements are applicable to experimental data without loss of generality.

Principal component analysis.— Fixing the value of U , we run PCA on samples generated for different values of V to explore fixed- U cuts of the phase diagram. As a dimensional reduction method, PCA projects samples onto directions of largest variance in the data. It has been applied to detect phase transitions based on Monte Carlo samples for classical and quantum models [30, 32, 72, 73].

We find that the spread of the projected samples at fixed V can be reduced, leading to a better resolution, if the input features \mathbf{x} contain N_c concatenated spin-resolved samples. Fig. 2 (a) shows the relative weight of the eigenvalues of the covariance matrix of data, which represents the variance along the principal components, for samples generated at $U = 6$ and different values of V for $N_c = 1$ and $N_c = 200$. The increase in concatenated features reveals only one relevant principal component. The inset of Fig. 2 (a) shows the average of the first principal component, revealing its average action on the spin-resolved occupancy as the π component of the Fourier transform of the total charge distribution. This

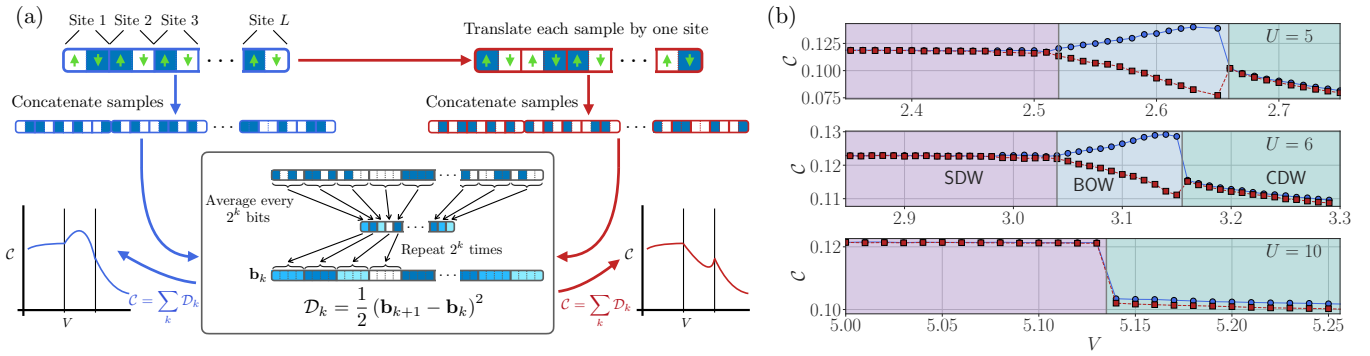


FIG. 3. (a) Procedure for computing the structural complexity. N_s samples are produced for a single ground state for a fixed value of U and V . The samples are then: concatenated together, or translated by one lattice site and concatenated together. The multi-scale structural complexity is computed for both resulting bitstrings. One coarse-graining step is shown in the box, consisting in the computation of the average of adjacent groups of 2^k bits. (b) Multi-scale structural complexity \mathcal{C} as a function of nearest-neighbor interaction V at fixed $U = 5$, $U = 6$, and $U = 10$. The connected blue circles and red squares correspond to the upper and lower branches of the complexity measure in the BOW phase. The two branches are obtained by computing the structural complexity from the samples extracted directly from the emulated ground-state wave function and the samples obtained after translation by one lattice site as shown in panel (a).

quantity is the order parameter for the CDW phase.

Fig. 2(b) shows the effect of the concatenation of the input features on their projection to the first two principal components. We observe that the first principal component resolves two clusters. The first one corresponding to samples in SDW and the BOW phases and the second one containing samples from the CDW phase. Fig. 2 (c) shows, for a fixed value of U and V , the average projection of the input features to the first and second principal components ($N_c = 200$). As expected by the connection of the first principal component with the CDW order parameter, PCA can only resolve the BOW-CDW phase transition and its nature, first- or second-order (see [68] for the PCA of the samples at different values of U). However, it shows no signal for the BKT-type transition between SDW and BOW phases.

Multi-scale structural complexity.— Recently, the multi-scale structural complexity measure [61] has been used to obtain off-diagonal information about quantum states through projective measurements in a single basis [62]. As shown schematically in Fig. 3 (a), the idea consists of concatenating all available samples for the same quantum state (creating a bitstring), performing several coarse-graining steps, and computing the dissimilarity \mathcal{D}_k between consecutive coarse-graining steps k and $k + 1$ [62, 68]. These dissimilarities are added except for the first step to obtain the so-called multi-scale structural complexity \mathcal{C} .

For each (U, V) point, the N_s spin-resolved samples are concatenated in two ways: (1) concatenation without shifting and (2) concatenation after translating all samples by one site (two bits with spin resolution) considering a periodic boundary for the bitstring. These form two sets of bitstrings of length $2 \cdot L \cdot N_s$ each.

As shown in Fig. 3 (b), the multi-scale structural complexity captures both phase transitions. The two sets of complexity analyses give essentially the same, almost constant, \mathcal{C} (up to a constant shift) inside the SDW phase. As V is increased, the transition to a BOW phase is clearly indicated by the splitting of the complexity measures into two branches. One branch increases as V is increased while the other branch decreases, corresponding to the two types of polarization of strong and weak kinetic energy bonds in the BOW phase. The higher (lower) value of \mathcal{C} is associated with a higher (lower) number of high kinetic energy bonds in the chain of length L . As we keep increasing V , the two branches collapse into a single curve, indicating the transition to the CDW phase. The absence of the BOW phase for $U = 10$ is indicated by the lack of bifurcation of the complexity measure.

It is worth noting that if we generate samples with equal probability from degenerate states in the BOW phase, the complexity does not bifurcate in the BOW phase like it does in Fig. 3 (b). This is shown in the Supplemental Materials [68]. It is then concluded that for the resolution of the BKT-type transition from the complexity analysis of single-basis projective measurements, we need samples that come from only one of the degenerate ground states. As discussed above, this can be achieved by imposing open boundary conditions [57, 68] or diagonal edge pinning fields [55, 74, 75].

Phase diagram— Fig. 1(c) compares the phase boundaries determined by the entanglement entropy \mathcal{S}_i (red triangles) with those determined using the structural complexity \mathcal{C} , computed from samples directly (blue squares). The complexity analysis gives accurate results and quantitatively agrees with the off-diagonal observables computed from the wave function in the TDL within er-

ror bars. Our results are also consistent with previous works [36, 52]. Furthermore, obtaining the ground-state wave function in the TDL and combining local observables with machine learning approaches can shed light on the challenges of quantitatively locating the BKT-type transition [52, 53, 55–57].

Conclusion.— In this work, we use the VUMPS algorithm to generate the 1D ground-state wave-function of the extended Hubbard model directly in the TDL, which allows us to determine phase boundaries with high precision without considering boundary effects and finite-size scaling. We sample real-space snapshots of finite length and use them along with unsupervised learning methods to characterize the BKT-type phase transition between SDW and BOW phases as well as the first-order and second-order phase transition between BOW and CDW phases. We find that off-diagonal long-range order cannot be detected by the PCA even after concatenation of samples. However, using the structural complexity analysis, the off-diagonal long-range order can be detected using spin-resolved fermion density snapshots if these snapshots are generated from one of the degenerate ground states of the BOW phase. We argue that in optical lattice experiments, this can be achieved by imposing open boundary conditions. Our results indicate the potential of machine learning techniques in revealing microscopic mechanisms and hidden orders using projective measurements of corresponding thermal density matrix in quantum gas microscopes. While detection of phases with off-diagonal long-range order using diagonal descriptors has been demonstrated, further work is required to see if ML methods such as multiscale complexity can also differentiate between BKT and second order transitions from which they emerge. Likewise, it should be noted that while the structural complexity effectively locates transitions, it does not directly yield the physical nature of the order.

Acknowledgement We are indebted to Andrew Millis for carefully reading the manuscript. We would like to thank Benedikt Kloss, Anders Sandvik, Miles Stoudenmire, Simon Trebst and Steven White for insightful discussions. Flatiron Institute is a division of the Simons Foundation. The work of E.K. and R.S. was supported by the grant DE-SC-0022311, funded by the U.S. Department of Energy, Office of Science. D.S. was supported by AFOSR: Grant FA9550-21-1-0236.

* bxiao@flatironinstitute.org

† jrm874@nyu.edu

- [1] J. F. Sherson, C. Weitenberg, M. Endres, M. Cheneau, I. Bloch, and S. Kuhr, Single-atom-resolved fluorescence imaging of an atomic Mott insulator, *Nature* **467**, 68 (2010).
- [2] W. S. Bakr, A. Peng, M. E. Tai, R. Ma, J. Simon, J. I. Gillen, S. Foelling, L. Pollet, and M. Greiner, Probing the superfluid-to-Mott insulator transition at the single-atom level, *Science* **329**, 547 (2010).
- [3] C. Gross and W. S. Bakr, Quantum gas microscopy for single atom and spin detection, *Nature Physics* **17**, 1316 (2021).
- [4] M. F. Parsons, A. Mazurenko, C. S. Chiu, G. Ji, D. Greif, and M. Greiner, Site-resolved measurement of the spin-correlation function in the Fermi-Hubbard model, *Science* **353**, 1253 (2016).
- [5] L. W. Cheuk, M. A. Nichols, K. R. Lawrence, M. Okan, H. Zhang, E. Khatami, N. Trivedi, T. Paiva, M. Rigol, and M. W. Zwierlein, Observation of spatial charge and spin correlations in the 2D Fermi-Hubbard model, *Science* **353**, 1260 (2016).
- [6] P. T. Brown, D. Mitra, E. Guardado-Sanchez, P. Schauß, S. S. Kondov, E. Khatami, T. Paiva, N. Trivedi, D. A. Huse, and W. S. Bakr, Spin-imbalance in a 2D Fermi-Hubbard system, *Science* **357**, 1385 (2017).
- [7] A. Mazurenko, C. S. Chiu, G. Ji, M. F. Parsons, M. Kanász-Nagy, R. Schmidt, F. Grusdt, E. Demler, D. Greif, and M. Greiner, A cold-atom Fermi-Hubbard antiferromagnet, *Nature* **545**, 462 (2017).
- [8] T. Hartke, B. Oreg, C. Turnbaugh, N. Jia, and M. Zwierlein, Direct observation of nonlocal fermion pairing in an attractive Fermi-Hubbard gas, *Science* **381**, 82 (2023).
- [9] P. Schauß, M. Cheneau, M. Endres, T. Fukuhara, S. Hild, A. Omran, T. Pohl, C. Gross, S. Kuhr, and I. Bloch, Observation of spatially ordered structures in a two-dimensional Rydberg gas, *Nature* **491**, 87 (2012).
- [10] S. Ebadi, T. T. Wang, H. Levine, A. Keesling, G. Semeghini, A. Omran, D. Bluvstein, R. Samajdar, H. Pichler, W. W. Ho, *et al.*, Quantum phases of matter on a 256-atom programmable quantum simulator, *Nature* **595**, 227 (2021).
- [11] P. Scholl, M. Schuler, H. J. Williams, A. A. Eberharter, D. Barredo, K.-N. Schymik, V. Lienhard, L.-P. Henry, T. C. Lang, T. Lahaye, *et al.*, Quantum simulation of 2D antiferromagnets with hundreds of Rydberg atoms, *Nature* **595**, 233 (2021).
- [12] R. Samajdar, W. W. Ho, H. Pichler, M. D. Lukin, and S. Sachdev, Complex density wave orders and quantum phase transitions in a model of square-lattice Rydberg atom arrays, *Phys. Rev. Lett.* **124**, 103601 (2020).
- [13] A. Browaeys and T. Lahaye, Many-body physics with individually controlled Rydberg atoms, *Nature Physics* **16**, 132 (2020).
- [14] H. Labuhn, D. Barredo, S. Ravets, S. De Léséleuc, T. Macrì, T. Lahaye, and A. Browaeys, Tunable two-dimensional arrays of single Rydberg atoms for realizing quantum Ising models, *Nature* **534**, 667 (2016).
- [15] H. Bernien, S. Schwartz, A. Keesling, H. Levine, A. Omran, H. Pichler, S. Choi, A. S. Zibrov, M. Endres, M. Greiner, *et al.*, Probing many-body dynamics on a

- 51-atom quantum simulator, *Nature* **551**, 579 (2017).
- [16] P. Mehta, M. Bukov, C.-H. Wang, A. G. Day, C. Richardson, C. K. Fisher, and D. J. Schwab, A high-bias, low-variance introduction to machine learning for physicists, *Physics Reports* **810**, 1 (2019).
- [17] G. Carleo, I. Cirac, K. Cranmer, L. Daudet, M. Schuld, N. Tishby, L. Vogt-Maranto, and L. Zdeborová, Machine learning and the physical sciences, *Rev. Mod. Phys.* **91**, 045002 (2019).
- [18] S. Johnston, E. Khatami, and R. Scalettar, A perspective on machine learning and data science for strongly correlated electron problems, *Carbon Trends* **9**, 100231 (2022).
- [19] A. Bohrdt, C. S. Chiu, G. Ji, M. Xu, D. Greif, M. Greiner, E. Demler, F. Grusdt, and M. Knap, Classifying snapshots of the doped Hubbard model with machine learning, *Nature Physics* **15**, 921 (2019).
- [20] E. Khatami, E. Guardado-Sanchez, B. M. Spar, J. F. Carrasquilla, W. S. Bakr, and R. T. Scalettar, Visualizing strange metallic correlations in the two-dimensional Fermi-Hubbard model with artificial intelligence, *Phys. Rev. A* **102**, 033326 (2020).
- [21] C. Miles, A. Bohrdt, R. Wu, C. Chiu, M. Xu, G. Ji, M. Greiner, K. Q. Weinberger, E. Demler, and E.-A. Kim, Correlator convolutional neural networks as an interpretable architecture for image-like quantum matter data, *Nature Communications* **12**, 1 (2021).
- [22] C. Miles, R. Samajdar, S. Ebadi, T. T. Wang, H. Pichler, S. Sachdev, M. D. Lukin, M. Greiner, K. Q. Weinberger, and E.-A. Kim, Machine learning discovery of new phases in programmable quantum simulator snapshots, *Physical Research* **5**, 013026 (2023).
- [23] B. S. Rem, N. Käming, M. Tarnowski, L. Asteria, N. Fläschner, C. Becker, K. Sengstock, and C. Weitenberg, Identifying quantum phase transitions using artificial neural networks on experimental data, *Nature Physics* **15**, 917 (2019).
- [24] N. Käming, A. Dawid, K. Kottmann, M. Lewenstein, K. Sengstock, A. Dauphin, and C. Weitenberg, Unsupervised machine learning of topological phase transitions from experimental data, *Machine Learning: Science and Technology* **2**, 035037 (2021).
- [25] L. Wang, Discovering phase transitions with unsupervised learning, *Phys. Rev. B* **94**, 195105 (2016).
- [26] J. Carrasquilla and R. G. Melko, Machine learning phases of matter, *Nature Physics* **13**, 431 (2017).
- [27] P. Broecker, J. Carrasquilla, R. G. Melko, and S. Trebst, Machine learning quantum phases of matter beyond the fermion sign problem, *Scientific reports* **7**, 1 (2017).
- [28] K. Ch'ng, J. Carrasquilla, R. G. Melko, and E. Khatami, Machine learning phases of strongly correlated fermions, *Phys. Rev. X* **7**, 031038 (2017).
- [29] Y. Zhang and E.-A. Kim, Quantum loop topography for machine learning, *Phys. Rev. Lett.* **118**, 216401 (2017).
- [30] W. Hu, R. R. P. Singh, and R. T. Scalettar, Discovering phases, phase transitions, and crossovers through unsupervised machine learning: A critical examination, *Phys. Rev. E* **95**, 062122 (2017).
- [31] E. P. Van Nieuwenburg, Y.-H. Liu, and S. D. Huber, Learning phase transitions by confusion, *Nature Physics* **13**, 435 (2017).
- [32] S. J. Wetzel and M. Scherzer, Machine learning of explicit order parameters: From the Ising model to SU(2) lattice gauge theory, *Phys. Rev. B* **96**, 184410 (2017).
- [33] M. J. S. Beach, A. Golubeva, and R. G. Melko, Machine learning vortices at the Kosterlitz-Thouless transition, *Phys. Rev. B* **97**, 045207 (2018).
- [34] J. F. Rodriguez-Nieva and M. S. Scheurer, Identifying topological order through unsupervised machine learning, *Nature Physics* **15**, 790 (2019).
- [35] Y. Miyajima, Y. Murata, Y. Tanaka, and M. Mochizuki, Machine learning detection of Berezinskii-Kosterlitz-Thouless transitions in q -state clock models, *Phys. Rev. B* **104**, 075114 (2021).
- [36] S. Ejima and S. Nishimoto, Phase diagram of the one-dimensional half-filled extended Hubbard model, *Phys. Rev. Lett.* **99**, 216403 (2007).
- [37] T. Ishiguro and K. Yamaji, *Organic Superconductors* (Springer, Berlin, Heidelberg, 1990).
- [38] E. Dagotto and T. Rice, Surprises on the way from one-to two-dimensional quantum magnets: the ladder materials, *Science* **271**, 618 (1996).
- [39] J. Hu, T. W. Odom, and C. M. Lieber, Chemistry and physics in one dimension: synthesis and properties of nanowires and nanotubes, *Accounts of chemical research* **32**, 435 (1999).
- [40] H. Ishii, H. Kataura, H. Shiozawa, H. Yoshioka, H. Otsubo, Y. Takayama, T. Miyahara, S. Suzuki, Y. Achiba, M. Nakatake, et al., Direct observation of Tomonaga-Luttinger-liquid state in carbon nanotubes at low temperatures, *Nature* **426**, 540 (2003).
- [41] S. Baier, M. J. Mark, D. Petter, K. Aikawa, L. Chomaz, Z. Cai, M. Baranov, P. Zoller, and F. Ferlaino, Extended Bose-Hubbard models with ultracold magnetic atoms, *Science* **352**, 201 (2016).
- [42] H. Shiba, Magnetic susceptibility at zero temperature for the one-dimensional Hubbard model, *Phys. Rev. B* **6**, 930 (1972).
- [43] M. Imada and Y. Hatsugai, Numerical studies on the Hubbard model and the t-J model in one-and two-dimensions, *Journal of the Physical Society of Japan* **58**, 3752 (1989).
- [44] H. J. Schulz, Correlation exponents and the metal-insulator transition in the one-dimensional Hubbard model, *Phys. Rev. Lett.* **64**, 2831 (1990).
- [45] P. Sengupta, A. W. Sandvik, and D. K. Campbell, Bond-order-wave phase and quantum phase transitions in the one-dimensional extended Hubbard model, *Phys. Rev. B* **65**, 155113 (2002).
- [46] R. T. Clay, S. Mazumdar, and D. K. Campbell, Pattern of charge ordering in quasi-one-dimensional organic charge-transfer solids, *Phys. Rev. B* **67**, 115121 (2003).
- [47] F. H. Essler, H. Frahm, F. Göhmann, A. Klümper, and V. E. Korepin, *The one-dimensional Hubbard model* (Cambridge University Press, 2005).
- [48] A. W. Sandvik and D. K. Campbell, Spin-Peierls transition in the Heisenberg chain with finite-frequency phonons, *Phys. Rev. Lett.* **83**, 195 (1999).
- [49] M. Nakamura, Tricritical behavior in the extended Hubbard chains, *Phys. Rev. B* **61**, 16377 (2000).
- [50] M. Tsuchizu and A. Furusaki, Phase diagram of the one-dimensional extended Hubbard model at half filling, *Phys. Rev. Lett.* **88**, 056402 (2002).
- [51] E. Jeckelmann, Ground-state phase diagram of a half-filled one-dimensional extended Hubbard model, *Phys. Rev. Lett.* **89**, 236401 (2002).
- [52] A. W. Sandvik, L. Balents, and D. K. Campbell, Ground state phases of the half-filled one-dimensional extended

- Hubbard model, *Phys. Rev. Lett.* **92**, 236401 (2004).
- [53] Y. Z. Zhang, Dimerization in a half-filled one-dimensional extended Hubbard model, *Phys. Rev. Lett.* **92**, 246404 (2004).
- [54] S. Ejima, F. H. L. Essler, F. Lange, and H. Fehske, Ising tricriticality in the extended Hubbard model with bond dimerization, *Phys. Rev. B* **93**, 235118 (2016).
- [55] J. Spalding, S.-W. Tsai, and D. K. Campbell, Critical entanglement for the half-filled extended Hubbard model, *Phys. Rev. B* **99**, 195445 (2019).
- [56] M. Dalmonte, J. Carrasquilla, L. Taddia, E. Ercolessi, and M. Rigol, Gap scaling at Berezinskii-Kosterlitz-Thouless quantum critical points in one-dimensional Hubbard and Heisenberg models, *Phys. Rev. B* **91**, 165136 (2015).
- [57] S. Julià-Farré, D. González-Cuadra, A. Patscheider, M. J. Mark, F. Ferlino, M. Lewenstein, L. Barbiero, and A. Dauphin, Revealing the topological nature of the bond order wave in a strongly correlated quantum system, *Phys. Rev. Research* **4**, L032005 (2022).
- [58] V. Zauner-Stauber, L. Vanderstraeten, M. T. Fishman, F. Verstraete, and J. Haegeman, Variational optimization algorithms for uniform matrix product states, *Phys. Rev. B* **97**, 045145 (2018).
- [59] V. Zauner-Stauber, L. Vanderstraeten, J. Haegeman, I. P. McCulloch, and F. Verstraete, Topological nature of spinons and holons: Elementary excitations from matrix product states with conserved symmetries, *Phys. Rev. B* **97**, 235155 (2018).
- [60] L. Vanderstraeten, J. Haegeman, and F. Verstraete, Tangent-space methods for uniform matrix product states, *SciPost Phys. Lect. Notes* , 7 (2019).
- [61] A. A. Bagrov, I. A. Iakovlev, A. A. Iliasov, M. I. Katsnelson, and V. V. Mazurenko, Multiscale structural complexity of natural patterns, *Proceedings of the National Academy of Sciences* **117**, 30241 (2020).
- [62] O. M. Sotnikov, I. A. Iakovlev, A. A. Iliasov, M. I. Katsnelson, A. A. Bagrov, and V. V. Mazurenko, Certification of quantum states with hidden structure of their bitstrings, *npj Quantum Information* **8**, 41 (2022).
- [63] J. Haegeman, J. I. Cirac, T. J. Osborne, I. Pizorn, H. Verschelde, and F. Verstraete, Time-dependent variational principle for quantum lattices, *Phys. Rev. Lett.* **107**, 070601 (2011).
- [64] J. Haegeman, C. Lubich, I. Oseledets, B. Vandereycken, and F. Verstraete, Unifying time evolution and optimization with matrix product states, *Phys. Rev. B* **94**, 165116 (2016).
- [65] I. P. McCulloch, Infinite size density matrix renormalization group, revisited, *arXiv preprint arXiv:0804.2509* (2008).
- [66] S. R. White, Density matrix formulation for quantum renormalization groups, *Phys. Rev. Lett.* **69**, 2863 (1992).
- [67] U. Schollwöck, The density-matrix renormalization group, *Rev. Mod. Phys.* **77**, 259 (2005).
- [68] See Supplemental Materials.
- [69] M. Fishman, S. R. White, and E. M. Stoudenmire, The ITensor software library for tensor network calculations (2020), *arXiv:2007.14822*.
- [70] S. R. White, Minimally entangled typical quantum states at finite temperature, *Phys. Rev. Lett.* **102**, 190601 (2009).
- [71] E. M. Stoudenmire and S. R. White, Minimally entangled typical thermal state algorithms, *New Journal of Physics* **12**, 055026 (2010).
- [72] L. Wang, Discovering phase transitions with unsupervised learning, *Phys. Rev. B* **94**, 195105 (2016).
- [73] E. Khatami, Principal component analysis of the magnetic transition in the three-dimensional Fermi-Hubbard model, *Journal of Physics: Conference Series* **1290**, 012006 (2019).
- [74] F. F. Assaad and I. F. Herbut, Pinning the order: The nature of quantum criticality in the Hubbard model on honeycomb lattice, *Phys. Rev. X* **3**, 031010 (2013).
- [75] B. Xiao, Y.-Y. He, A. Georges, and S. Zhang, Temperature dependence of spin and charge orders in the doped two-dimensional Hubbard model, *Phys. Rev. X* **13**, 011007 (2023).
- [76] R. Orús, A practical introduction to tensor networks: Matrix product states and projected entangled pair states, *Annals of Physics* **349**, 117 (2014).
- [77] M. M. Rams, P. Czarnik, and L. Cincio, Precise extrapolation of the correlation function asymptotics in uniform tensor network states with application to the Bose-Hubbard and XXZ models, *Phys. Rev. X* **8**, 041033 (2018).
- [78] L. Tagliacozzo, T. R. de Oliveira, S. Iblisdir, and J. I. Latorre, Scaling of entanglement support for matrix product states, *Phys. Rev. B* **78**, 024410 (2008).
- [79] F. Pollmann, S. Mukerjee, A. M. Turner, and J. E. Moore, Theory of finite-entanglement scaling at one-dimensional quantum critical points, *Phys. Rev. Lett.* **102**, 255701 (2009).
- [80] B. Pirvu, G. Vidal, F. Verstraete, and L. Tagliacozzo, Matrix product states for critical spin chains: Finite-size versus finite-entanglement scaling, *Phys. Rev. B* **86**, 075117 (2012).

Supplemental Materials: Extracting Off-Diagonal Order from Diagonal Basis Measurements

Bo Xiao¹, Javier Robledo Moreno^{1,2}, Matthew Fishman¹ Dries Sels^{1,2}, Ehsan Khatami³, and Richard Scalettar⁴

¹*Center for Computational Quantum Physics, Flatiron Institute,
162 Fifth Avenue, New York, New York 10010 USA*

²*Department of Physics, New York University, New York, New York 10003, USA*

³*Department of Physics and Astronomy, San José State University, San José, CA 95192*

⁴*Department of Physics and Astronomy, University of California, Davis, CA 95616 USA*

PRINCIPAL COMPONENT ANALYSIS

PCA computes the eigenvalues λ_k and eigenvectors $\mathbf{w}^{(k)}$ of the covariance matrix of the samples. Then, the samples are projected onto the eigenvectors with the largest eigenvalues according to $y_k = \mathbf{x} \cdot \mathbf{w}^{(k)}$. In Fig. 2 of the main text, we show the normalized eigenvalues, the eigenvector corresponding to the largest eigenvalue, and projections of data onto the first two principal components.

CORRELATION LENGTH AND VON NEUMANN ENTANGLEMENT ENTROPY

Tensor network techniques allow us to efficiently approximate the state of systems composed of many degrees of freedom with a manageable number of relevant ones. For matrix product states (MPS), the connected correlation function asymptotically decays exponentially with distance [76, 77]

$$C(r) \sim e^{-r/\xi}. \quad (1)$$

The correlation length can be computed using the transfer matrix \mathcal{T}

$$\xi = -\frac{1}{\log |\lambda_2/\lambda_1|}, \quad (2)$$

where $|\lambda_1| > |\lambda_2| \geq |\lambda_3| \geq \dots \geq |\lambda_D|$ are the eigenvalues of \mathcal{T} and D is the bond dimension [76].

As shown in panel (a) of Fig. S1, the correlation length ξ is large and grows with the bond dimension in the SDW phase (which is spin gapless) and diverges exactly at the continuous phase transition between the CDW and the BOW phase. In sharp contrast, the correlation length ξ has negligible dependence on the bond dimension and remains short distance in the CDW in which both the charge and spin excitation are gapped. Inside the BOW, ξ has clear dependence on the bond dimension near the BKT-type transition and gradually becomes bond dimension independent.

In addition to the correlation length ξ , the entanglement entropy is also a measure of correlations [78–80]. The von Neumann entropy of a pure state of a bipartite system AB is defined as,

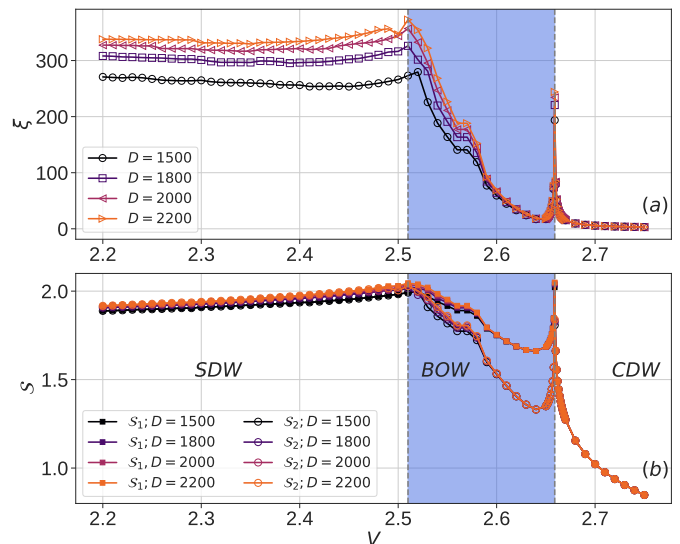


FIG. S1. (a) Correlation length ξ and (b) entanglement entropy S vs. nearest-neighbor interaction V with fixed $U = 5$ using different bond dimensions. The second-order phase transition from BOW to CDW is located at $V_{c2} = 2.659$, where sharp peaks in ξ and S are observed. The BKT-type transition from SDW to BOW is located $V_{c1} = 2.52$.

$$S = -\text{Tr} \rho_A \log \rho_A = -\text{Tr} \rho_B \log \rho_B \quad (3)$$

where ρ_A (ρ_B) is the reduced density matrix of subsystem A (B). Inside a two-site unit cell, there are two bonds, along which we can divide an infinite chain into two half-infinite chains and then compute the entanglement entropy. We denote the entanglement entropies computed by these two divisions S_1 and S_2 correspondingly, as shown in Fig. S1.

In panel (b) of Fig. S1, we show how the von Neumann entanglement entropy S evolves along a vertical cut with $U = 5$ fixed on the phase diagram shown in Fig. 1(c). The entanglement entropy peaks exactly at the BKT-type and continuous quantum phase transitions. In the CDW phase, S decreases rapidly below $S = 1$ as V is increased, which indicates the system becoming more and more classical. Most importantly, given the broken translational invariance in the BOW phase, the two entangle-

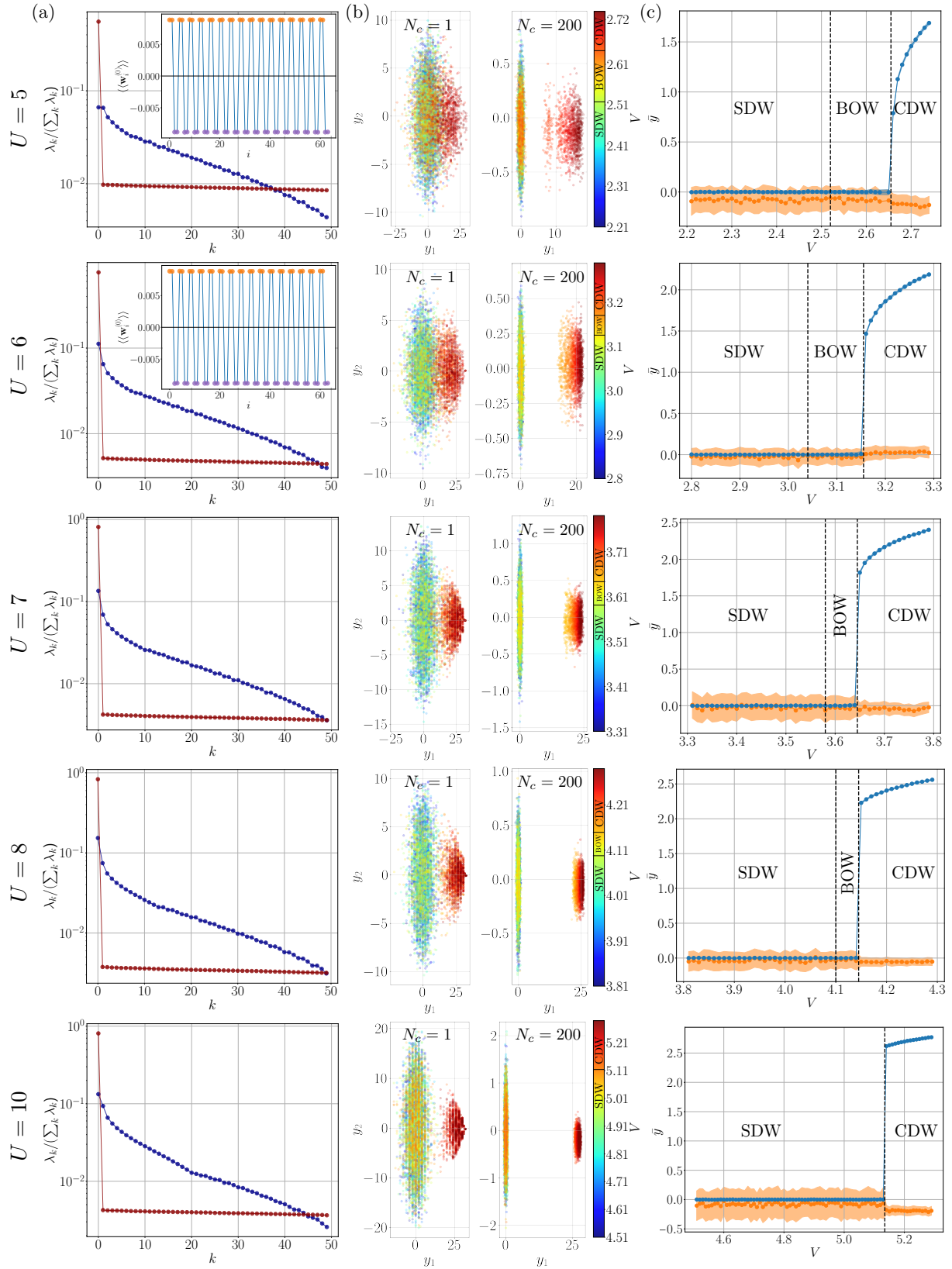


FIG. S2. Principal component analysis of the samples generated at $U = 5, 6, 7, 8, 10$ as indicated on each row of figures and different values of V on a uniform grid with separation $\Delta V = 0.1$. (a) Explained variance ratio measured by the relative weight of the eigenvalues of covariance matrix of data comparing two values of concatenated samples N_c . The inset shows the amplitude of the first principal component for $N_c = 200$, averaged over the concatenated samples. (b) Projection of the input features to the first two principal components both when $N_c = 1$ and $N_c = 200$. The color indicates the value of V to which each projected feature belongs. (c) Average projection of the input features to the first (blue) and second (orange) principal components for $N_c = 200$. The shaded region shows the variance of the average value, measuring the spread of the projected input features at a fixed V . Vertical dashed lines indicate the phase transition points obtained from the entanglement entropy.

ment entropies deviate from each other, which reflects the \mathcal{Z}_2 degeneracy of two types of polarization.

PCA FOR ALL U VALUES CONSIDERED IN THIS STUDY.

This section shows the results obtained from PCA at different values of U . Panel (a) of Fig. S2 shows the variance ratio, defined as the relative weight of the eigenvalues of the covariance matrix, for $N_c = 1$ and $N_c = 200$. The effect of increasing the number of concatenated samples on the input features is to improve the resolution of the variance profile in the space defined by the samples. For $N_c = 200$, only one principal component is necessary to describe the variance properties of the data, for every value of U . As shown by the inset on panel (a) of Fig. S2, the first principal component is nearly identical for all values of U . As discussed in the main text, this particular profile for the first principal component computes the CDW order parameter for the samples.

Fig. S2 (b) shows the input features projected to the first two principal components for $N_c = 1$ and $N_c = 200$. In both cases, two clusters are resolved along the first principal component. The first cluster corresponds to samples that belong to SDW and BOW phases, while the second cluster contains mostly samples that belong to the CDW phase. The effect of increasing the number of concatenated samples of the input features is to provide a better distinction between the two clusters.

Panel (c) in Fig. S2 shows, for five fixed values of U and V , the average projection to the first and second principal components of the input features for $N_c = 200$. For all values of U the average projection as a function of V remains featureless in the SDW and BOW phases, and increases rapidly in the CDW phase. It must be noted that this rapid increase is continuous at $U = 5$, while it is discontinuous at $U = 6, 7, 8, 10$, reflecting the second ($U = 5$) and first ($U = 6, 7, 8, 10$) order nature of the BOW-CDW transition. This observation comes as no surprise at the projection of the input features to the first principal component is analogous to the computation of the CDW order parameter.

STRUCTURAL COMPLEXITY OF SAMPLES WITH MIXED POLARIZATIONS

In the main text, we show how to apply the structural complexity analysis to samples that are drawn from the same \mathcal{Z}_2 degenerate ground state. When periodic boundary conditions (PBC) are used or the TDL is reached, sampling from one specific state among degenerate states is not possible. In Fig. S3(a), we show results of the structural complexity when samples drawn from different degenerate ground states are mixed. In the BOW and

CDW states, we sample the two-fold degenerate ground-state wavefunctions simultaneously and select samples as the input data with equal probability. As a result, the structural complexity is featureless near the quantum phase transition from SDW to BOW. No kink or sudden change of slope is observed, compared to the case where samples with different polarizations are not mixed. In contrast, the structural complexity is still able to capture the second-order transition from BOW phase to CDW phase, although the signal is weaker when samples are selected from both degenerate states.

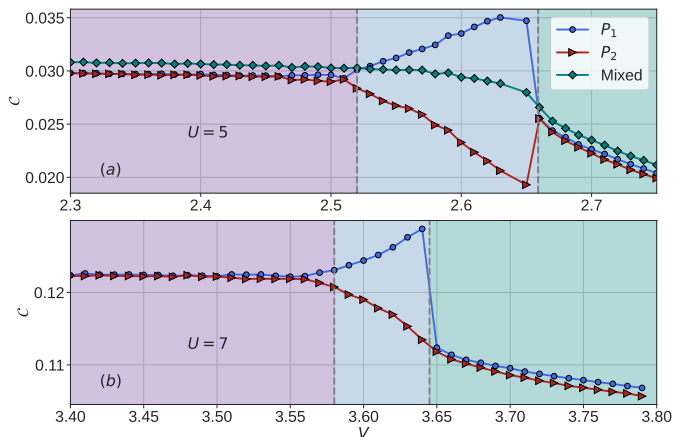


FIG. S3. Multi-scale structural complexity \mathcal{C} as a function of nearest-neighbor interaction V at fixed (a) $U = 5$ and (b) $U = 7$. Blue circles and red triangles are results obtained by analyzing samples drawn from single ground state selected from the \mathcal{Z}_2 degenerate ground states. Teal diamonds show results when samples are drawn from both of the degenerate states with equal probability.

As shown in Fig. S3(b), the details of how the lower branch of the structural complexity transits from the BOW phase to CDW phase as V is increased depends on the nature of BOW to CDW transition. For a second-order transition, e.g., at $U = 5$, the lower branch shows a dip before entering the CDW phase. In contrast, if the transition is first-order, e.g., at $U = 7$, there is no dip appearing in the lower branch.

WEAK-COUPLING REGIME

In the main text, our analysis centers on the intermediate- to strong-coupling regime, characterized by on-site interaction strengths of $U = 5$, $U = 6$, and $U = 10$. Drawing on the findings of previous studies [36, 55], we posit that between $U = 5$ and $U = 6$, the system approaches a tri-critical point where the transition between BOW and CDW shifts from a second-order to a first-order transition. At $U = 10$, a direct first-order transition from SDW to CDW is anticipated, bypassing the BOW phase entirely.

To validate the efficacy of our methodology, we have calculated the ground-state wave function at weak coupling, specifically for $U = 2$. As shown in Fig. S4(a)-(b), E_{B_ℓ} and S_{vN} enable the identification of both BKT-type and second-order phase transitions with great precision. Fig. S4(c) shows that the structural complexity is again able to pinpoint both phase boundaries in this case. Hence, we find the VUMPS algorithm and the complexity analysis remain robustly effective even when, at $U = 2$, the BOW phase is exceedingly narrow.

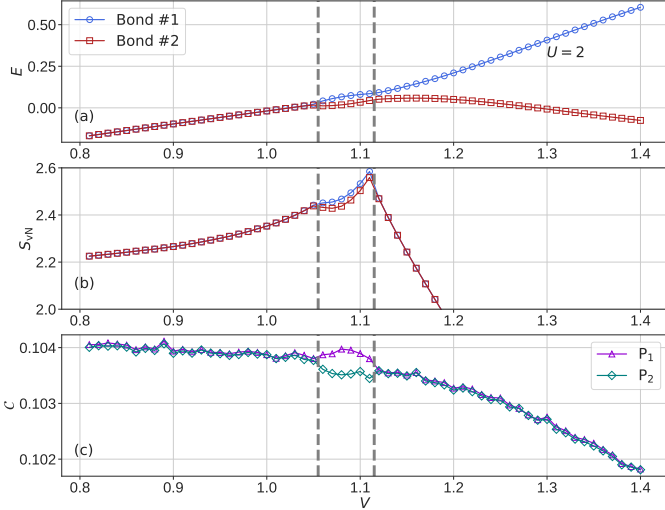


FIG. S4. In the weak-coupling regime, we investigate: (a) the energy E_ℓ , (b) the von Neumann entanglement entropy S_{vN} per bond for a single two-site unit cell at a constant on-site interaction strength of $U = 2$, and (c) the complexity analysis of samples derived from sampling the ground-state wave function.

OPEN BOUNDARY CONDITIONS AND THE BOW ORDER

Using exact diagonalization (ED) on finite systems we demonstrate that open boundary conditions (OBC) pin the bond order wave patterns in one dimensional chains as long as the number of sites of the chain L is even.

Fig. S5 shows the kinetic energy on each bond between chain sites i and $i + 1$, both for open and periodic boundary conditions, at two points in the phase diagram belonging to the BOW phase. When the boundary conditions are chosen to be periodic, the ground state found by ED is the uniform mixture between the two \mathcal{Z}_2 degenerate ground states of alternating high and low kinetic energy bonds. This translates into a flat profile of kinetic energy across the chain. For open boundary conditions, alternating bonds show a pattern of alternating high and low kinetic energies. The edges of the chain always have high kinetic energy (strong bond).

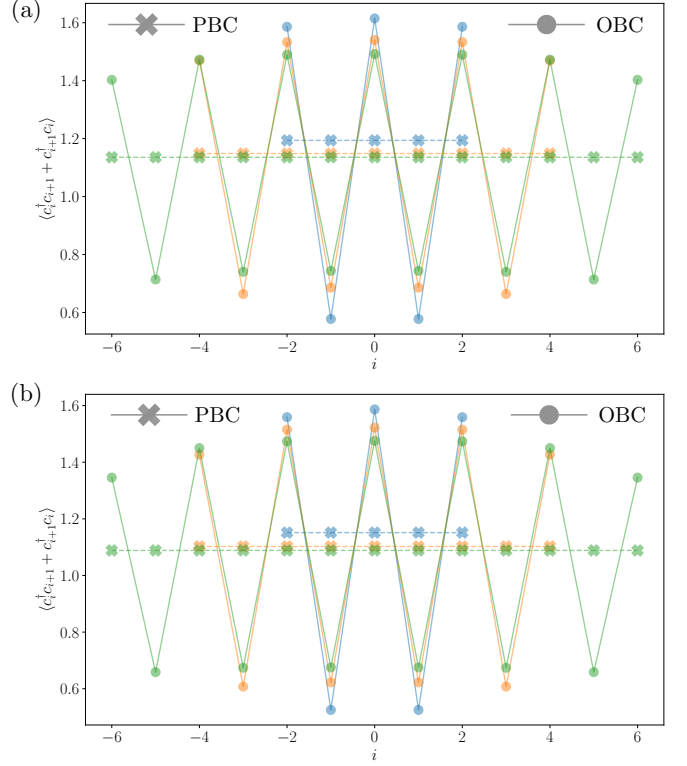


FIG. S5. Kinetic energy between sites i and $i + 1$ at each bond of the one-dimensional lattice, both for open boundary conditions and periodic boundary conditions. Panels (a) and (b) correspond to $(U = 5; V = 2.58)$ and $(U = 6; V = 3.08)$ respectively. Both points are inside the BOW phase. Different chain lengths are shown: blue ($L = 6$), orange ($L = 10$) and green ($L = 14$).

This can be explained by the following argument: OBC are the pinning field of infinite amplitude for BOW. OBC can be understood as forcing the kinetic energy at both bonds just outside of the chain to be zero. If the phase of the system is that of alternating high and low kinetic energies on neighboring bonds, it is easy to convince oneself that for even L , the kinetic energies at the end bonds of the chain have to be high. Furthermore, at fixed particle number, the kinetic energy is a semi-definite negative term in the Hamiltonian (it lowers the energy). For L even, the number of strong kinetic energy terms (negative terms) is maximized by having the bonds on both edges to have high kinetic energy. Therefore, that configuration of kinetic energy bonds is the one that lowers the energy, and therefore the true ground state of the system.